Atmos. Chem. Phys. Discuss., 11, 32685–32721, 2011
www.atmos-chem-phys-discuss.net/11/32685/2011/
doi:10.5194/acpd-11-32685-2011

Atmospheric Chemistry and Physics Discussions

Interpretation of FRESCO cloud retrievals in case of absorbing aerosol events

P. Wang, O. N. E. Tuinder, L. G. Tilstra, and P. Stammes

Royal Netherlands Meteorological Institute (KNMI), De Bilt, The Netherlands

Received: 17 October 2011 – Accepted: 2 December 2011 – Published: 12 December 2011

Correspondence to: P. Wang (wangp@knmi.nl)

Published by Copernicus Publications on behalf of the European Geosciences Union.

Abstract

Cloud and aerosol information is needed in trace gas retrievals from satellite measurements. The Fast REtrieval Scheme for Clouds from the Oxygen A band (FRESCO) cloud algorithm employs reflectance spectra of the O_2 A band around 760 nm to derive cloud pressure and effective cloud fraction. In general, clouds contribute more to the O_2 A band reflectance than aerosols. Therefore, the FRESCO algorithm does not correct for aerosol effects in the retrievals and attributes the retrieved cloud information entirely to the presence of clouds, and not to aerosols. For events with high aerosol loading, aerosols may have a dominant effect, especially for almost cloud-free scenes. We have analysed FRESCO cloud data and Absorbing Aerosol Index (AAI) data from the Global Ozone Monitoring Experiment (GOME-2) instrument on the Metop-A satellite for events with typical absorbing aerosol types, such as volcanic ash, desert dust and smoke. We find that the FRESCO effective cloud fractions are correlated with the AAI data for these absorbing aerosol events and that the FRESCO cloud pressures contain information on aerosol layer pressure. For cloud-free scenes, the derived FRESCO cloud pressures are close to those of the aerosol layer for optically thick aerosols. For cloudy scenes, if the strongly absorbing aerosols are located above the clouds, then the retrieved FRESCO cloud pressures may represent the height of the aerosol layer rather than the height of the clouds. Combining FRESCO cloud data and AAI, an estimate for the aerosol layer pressure can be given, which can be beneficial for aviation safety and operations in case of e.g. volcanic ash plumes.

1 Introduction

Cloud and aerosol information is relevant for the trace gas retrievals from satellite spectrometers like the Scanning Imaging Absorption Spectrometer for Atmospheric CHartographY (SCIAMACHY) on Envisat (Bovensmann et al., 1999) and the Global Ozone Monitoring Experiment (GOME-2) on Metop-A (Munro et al., 2006). Cloud products are

ACPD
11, 32685–32721, 2011

used to screen cloudy pixels or to correct for the effects of clouds on the trace gas retrievals. Various algorithms have been developed to retrieve cloud parameters from the SCIAMACHY and GOME-2 oxygen A band spectral measurements (e.g. Koelemeijer et al., 2001; Kokhanovsky et al., 2006) and from the PMD (Polarization Measurement Device) imagery measurements (Loyola, 2004; Grzegorski et al., 2006).

The Fast Retrieval Scheme for Clouds from the Oxygen A band (FRESCO) cloud retrieval algorithm has been developed as a simple but fast and robust algorithm for GOME, SCIAMACHY and GOME-2 (Koelemeijer et al., 2001; Wang et al., 2008). FRESCO employs the reflectance spectrum of the O_2 A band at 760 nm to derive effective cloud fraction and cloud pressure. Aerosols are treated in the same way as clouds in FRESCO, because clouds have much larger effects on the O_2 A band reflectances than aerosols in cloudy scenes. FRESCO cloud pressures have been validated with ground-based lidar/radar measurements (Wang et al., 2008). The FRESCO cloud product has not been investigated for events with high aerosol loading. It is well-known that the O_2 A band is suitable for the retrieval of aerosol height for cloud-free scenes (Dubuisson et al., 2009; Boesche et al., 2009). Therefore, it is interesting to know if there is any aerosol information in the FRESCO cloud product, and how to interpret it.

The Absorbing Aerosol Index (AAI), derived from UV reflectances, is an operational product of SCIAMACHY, GOME-2 and OMI (Ozone Monitoring Instrument) (De Graaf et al., 2005; Tilstra et al., 2010; Torres et al., 2007). The aerosol types that are mostly seen in the AAI data are desert dust, biomass burning smoke and volcanic ash aerosols. The AAI is hardly sensitive to clouds; therefore it is derived for both clear-sky and cloudy scenes (Torres et al., 1998; De Graaf et al., 2005). It is not straightforward to use the AAI quantitatively, because the AAI is sensitive to aerosol layer height, aerosol optical thickness, and single scattering albedo (Torres et al., 1998; De Graaf et al., 2005). If the aerosol layer height is known, the aerosol optical thickness can in principle be derived from the AAI (Torres et al., 1998). The AAI has been extensively used in the studies of biomass burning aerosols, desert dust and volcanic ash

ACPD
11, 32685–32721, 2011

plumes (e.g. Kaufman et al., 2005; Fromm et al., 2006; Eckardt and Kuring, 2005; Dirksen et al., 2009; De Graaf et al., 2010a; Guan et al., 2010; Witte et al., 2011). The GOME-2 AAI product is also used to support the Volcano Ash Advisory Centres (VAAC, http://www.temis.nl/o3msaf/vaac/).

In this study we focus on the interpretation of the FRESCO cloud product for strongly absorbing aerosol events, especially desert dust, biomass burning smoke, and volcanic ash plumes. We attempt to quantify the aerosol information in the FRESCO cloud product. Also, we want to know how to interpret the retrieved cloud information in the case of strongly absorbing aerosol events. In order to identify aerosol events we use the AAI as an indicator. We first analyse FRESCO cloud data using simulated spectra with absorbing aerosols and then analyse FRESCO data from GOME-2 measurements for the selected events. The structure of the paper is as follows. The GOME-2 FRESCO and AAI data and the method used in the analysis are described in Sect. 2. In Sect. 3 we simulate the effect of absorbing aerosols on the retrieved cloud height and effective cloud fraction. Section 4 presents the analysis of GOME-2 retrieval results for scenes containing volcanic ash plumes, Saharan desert dust, biomass burning smoke in West Africa, and Russian wild fires. In Sect. 5 conclusions are given.

2 Data sets and methodology

2.1 FRESCO cloud data

GOME-2 is onboard the Metop-A satellite of EUMETSAT. Metop-A is a sun-synchronised polar orbiting satellite with an overpass time of 09:30 local time (LT) at the equator. The swath width of the GOME-2 instrument is 1920 km with a pixel size of $40 \times 80\,km^2$. The GOME-2 spectrum covers the wavelength range 240–790 nm (Munro et al., 2006). The GOME-2 level 1 cloud product is based on the FRESCO algorithm (Wang and Stammes, 2007). In this analysis we use an improved FRESCO algorithm, FRESCO version 6 (v6).

ACPD
11, 32685–32721, 2011

In order to simulate the reflectance spectrum of a partly cloudy pixel inside and outside the O_2 A band, a simple atmospheric model is used, in which the atmosphere above the ground surface (for the clear-sky part of the pixel) or cloud (for the cloudy part of the pixel) is treated as an absorbing (due to oxygen) and purely Rayleigh scattering medium. Reflection occurs only at the surface and the cloud top. Surface and cloud are assumed to be Lambertian reflectors. The reflectance $R_{\mathrm{sim}}(\lambda, \theta, \theta_0, \phi-\phi_0)$ at wavelength λ, viewing zenith angle θ, solar zenith angle (SZA) θ_0, and relative azimuth angle $\phi-\phi_0$ is then given by Eq. (1),

$$R_{\mathrm{sim}} = cT_{\mathrm{c}}(z_{\mathrm{c}})A_{\mathrm{c}} + cR_{\mathrm{c}}(z_{\mathrm{c}}) + (1-c)T_{\mathrm{s}}(z_{\mathrm{s}})A_{\mathrm{s}} + (1-c)R_{\mathrm{s}}(z_{\mathrm{s}}). \quad (1)$$

If $c = 1$, the surface related terms vanish and Eq. (1) is simplified to Eq. (2),

$$R_{\mathrm{sim}} = T_{\mathrm{c}}(z_{\mathrm{sc}})A_{\mathrm{sc}} + R_{\mathrm{c}}(z_{\mathrm{sc}}). \quad (2)$$

Note that the wavelength and angle dependences are omitted in Eqs. (1, 2) for R_{sim}, T_{c}, R_{c}, T_{s}, and R_{s}. In the above equations, c is the effective cloud fraction, A_{c} is the cloud albedo, A_{s} is the surface albedo, and A_{sc} is the scene albedo. $T(\lambda, z_{\mathrm{s}}, \theta, \theta_0)$, $T(\lambda, z_{\mathrm{c}}, \theta, \theta_0)$, and $T(\lambda, z_{\mathrm{sc}}, \theta, \theta_0)$ are the direct atmospheric transmittances for light entering the atmosphere from the solar direction, propagating down to different levels with surface height z_{s}, cloud height z_{c}, and scene height z_{sc}, respectively, then propagating to the top of the atmosphere in the direction of the satellite. The O_2 absorption and single Rayleigh scattering are taken into account in the light paths for the transmitances and the single Rayleigh scattering reflectances above the cloud (R_{c}) and the surface (R_{s}), respectively (Wang et al., 2008). The transmittances and reflectances are pre-calculated and stored in look-up tables (LUT).

In FRESCO v6, effective cloud fraction, cloud pressure (or cloud height), scene albedo and scene pressure (or scene height) are derived for every pixel. Scene albedo and scene pressure were already retrieved in previous FRESCO versions but only for pixels flagged as having snow/ice on the surface. In the FRESCO algorithm, the cloud height, scene height and surface height are converted to cloud pressure, scene

ACPD
11, 32685–32721, 2011

pressure and surface pressure using the mid-latitude summer atmospheric profile (Anderson et al., 1986). Therefore, in FRESCO products the terms "height" and "pressure" are interchangeable. The effective cloud fraction and cloud pressure (cloud height) are retrieved using Eq. (1), whereas the cloud albedo is assumed to be 0.8, because cloud albedo and cloud fraction information cannot be separated from the O_2 A band spectra due to the large pixel size of GOME-2 and other similar satellite spectrometers. Surface albedo and surface height are taken from auxiliary databases.

Using Eq. (2), the scene albedo and scene pressure are derived by assuming the cloud fraction to be 1 (Koelemeijer et al., 2001; Stammes et al., 2008; Wang et al., 2008). Large aerosol plumes often cover several GOME-2 pixels. Thus, it seems reasonable to assume an aerosol or cloud fraction of 1 in these situations. The retrieved scene pressure and scene albedo are a radiance-weighted average of the cloudy and cloud-free parts of the pixels, because the GOME-2 pixels are often partly cloudy (Krijger et al., 2005). If a pixel is fully covered with clouds having optical thickness larger than about 35, the FRESCO scene pressure is the same as the cloud pressure.

The FRESCO v6 algorithm is an upgrade of the FRESCO+ (or FRESCO v5) algorithm using new databases and providing more output data (Wang and van der A, 2011; Wang et al., 2011). FRESCO v6 uses the high spatial resolution ($0.25^\circ \times 0.25^\circ$) surface albedo climatology derived from MERIS (Popp et al., 2011) and the latest O_2 line parameters from the HITRAN 2008 database (Rothman et al., 2009). Therefore, the effective cloud fraction and cloud pressure are retrieved more accurately. Because the absorption in the O_2 A band is slightly stronger in HITRAN 2008 than in HITRAN 2004, the FRESCO v6 global mean cloud pressure is about 10 hPa lower than for FRESCO v5. The HITRAN database change has no effect on the FRESCO effective cloud fraction. The difference between the effective cloud fraction in FRESCO v6 and v5 is entirely due to the MERIS surface albedo (Popp et al., 2011). The MERIS surface albedo is only available over land; over ocean the GOME surface albedo ($1^\circ \times 1^\circ$) is used (Koelemeijer et al., 2003). Thus, in FRESCO v6 the effective cloud fraction is expected to be improved with respect to v5 mainly over land and at coastal regions.

ACPD
11, 32685–32721, 2011

2.2 Absorbing Aerosol Index data

The operational GOME-2 Absorbing Aerosol Index (AAI) product is derived from the 340/380 nm wavelength pair (Tilstra et al., 2010; De Graaf et al., 2010b). The part of the reflectance spectrum that contains this wavelength pair is measured simultaneously with the O_2 A band spectrum from which the FRESCO cloud products are derived. As a result, the GOME-2 AAI and FRESCO data are collocated. The main advantage of the AAI over other aerosol detection techniques is its ability to detect absorbing aerosols over both land and sea surfaces, even in the presence of clouds. The latter property makes it very suited for the analysis performed in this paper.

The AAI has been shown to be sensitive to aerosol type, aerosol optical thickness (AOT), aerosol layer height, scattering geometry, and surface height (De Graaf et al., 2005). From this list of parameters, the aerosol layer height and the aerosol optical thickness are the most dominant. Generally speaking, aerosol plumes with large optical thickness and/or located at higher altitudes produce larger AAI values than plumes that are optically thin or are close to the surface (De Graaf et al., 2005; Torres et al., 1998; Jeong and Hsu, 2008).

Next to the operational GOME-2 AAI product derived from the main spectral channels at $80 \times 40\,km^2$ resolution, an experimental AAI product derived from the broadband PMDs is currently under development. This product offers an 8× higher spatial resolution ($10 \times 40\,km^2$) and a lower noise level. In the analyses we will mainly make use of the operational AAI values obtained from the main spectral channels. However, the AAI images we will show are derived from the experimental AAI product based on the PMD measurements.

2.3 MODIS data

The Moderate Resolution Imaging Spectroradiometer (MODIS) onboard the NASA EOS Terra satellite has an equator overpass time of 10:30 LT, which is about 1 h later than GOME-2 (09:30 LT). The time difference between MODIS and GOME-2

ACPD
11, 32685–32721, 2011

measurements is smaller at higher latitudes. We assume that the aerosol and cloud fields seen by MODIS and GOME-2 are similar. The MODIS RGB images and fire counts maps are used to visually determine the cloud amount and the location of the aerosol plume.

2.4 Methodology

In order to understand the FRESCO product for aerosol events, we first investigate the FRESCO product using simulated O_2 A band spectra for scenes containing aerosols and clouds. Next, strong absorbing aerosol events are selected from GOME-2 AAI global maps for 2010 and 2011 with AAI values larger than 4. In order to get a more significant statistic, we choose aerosol plumes with an extent of several degrees in latitude and longitude. In the analysis we select four typical events with absorbing aerosols: a volcanic ash plume event, a desert dust event, a biomass burning smoke event, and a wild fire smoke event. For all the selected aerosol events we also verify the plumes using the corresponding MODIS/Terra images. The analysis is based on the sensitivity of the AAI to the aerosol layer height and aerosol optical thickness. For every event we study the relationship between GOME-2 AAI and GOME-2 FRESCO effective cloud fraction, cloud pressure, scene albedo and scene pressure, respectively. If the AAI values are closely linked to the effective cloud fractions and/or scene albedos, then these two FRESCO products may contain aerosol optical thickness information. If the AAI values are correlated with FRESCO cloud pressures and/or scene pressures, then these FRESCO products may contain information on aerosol height. If there are no clouds in the scenes, the FRESCO products could simply be considered aerosol products.

ACPD
11, 32685–32721, 2011

3 FRESCO retrievals using simulated spectra of scenes containing clouds and aerosols

The O_2 A band spectra were simulated using the Doubling Adding KNMI (DAK) code (De Haan et al., 1987; Stammes, 2001) for four aerosol cases with aerosol optical thickness (AOT) of 0.5 and 3.65 and single scattering albedo (SSA) of 0.6 and 0.8, respectively. According to Johnson et al. (2008) the single scattering albedo of biomass burning aerosols is normally between 0.6 and 0.9, indicating that the SSA values used here are in a reasonable range. The aerosol layer was between 9 and 10 km. For the cloudy case, a cloud layer was set below the aerosol layer, between 1 and 2 km with a cloud optical thickness (COT) of 20. We set the aerosol layer above the cloud layer because if the aerosol layer is below the clouds, it may not be observed from satellite, particularly for optically thick cloud cases (De Graaf et al., 2005). The surface albedo was assumed to be 0.05 in all the simulations. The Henyey-Greenstein scattering phase function was used for both aerosols and clouds. The asymmetry parameter was 0.7 for aerosols and 0.85 for clouds. The single scattering albedo of clouds was assumed to be 1. The solar zenith angle (SZA) range was 0–75° and the viewing direction in the simulations was nadir. The scenes were assumed to be fully covered with aerosols or aerosols and clouds. The FRESCO cloud algorithm (v6) was applied to the simulated spectra to retrieve effective cloud fraction, cloud height, scene albedo, and scene height. The results are shown in Fig. 1 for the clear-sky cases and in Fig. 2 for the cloudy cases.

For the clear-sky cases, one would expect FRESCO to be able to retrieve aerosol height and effective aerosol fraction. As shown in Fig. 1a, the cloud (aerosol) heights in the standard retrieval are either 0 or 15 km for the four aerosol cases, which is not realistic because 0 and 15 km are the lower and upper limits in the FRESCO cloud height retrieval. In order to simulate a large O_2 absorption, FRESCO has to put the cloud at a low height, while the calculated reflectances and transmittances are constrained by the surface height, surface albedo, and cloud albedo (see Eq. 1). If the simulation with the

ACPD
11, 32685–32721, 2011

cloud at the surface height still produces less O_2 absorption than in the measurements, so that R_{sim} is too large at the O_2 A band center, the retrieval will not be performed correctly and the retrieved cloud height can be either 0 or 15 km. Figure 1c shows that the effective cloud (aerosol) fractions are mostly in a reasonable range. However, for the case with AOT = 3.65 and SSA = 0.6, the reflectances are very low; at small SZA the reflectances are even lower than for an aerosol-free scene. Therefore, in some cases the effective cloud fraction shows slightly negative values. The effective cloud fraction could be retrieved properly for aerosols with SSA = 0.8 because in this case the absorption is not too large.

As shown in Fig. 1b and d, the scene height is properly retrieved and the scene albedo has a reasonable value. For the cases with AOT = 3.65 and SSA = 0.6, 0.8, the retrieved scene heights are close to the aerosol layer height. For the cases with AOT = 0.5 and SSA = 0.6, 0.8, the retrieved scene heights are below the aerosol layer, although increasing to 8 km for large SZA. For the optically thick aerosol cases (AOT = 3.65), most photons are absorbed by the aerosol layer and the light path is not affected by the surface reflection, therefore the retrieved scene height corresponds closely to the height of the aerosol layer. The scene height increases with solar zenith angle which can also be explained by the longer slant light paths at large SZA which is similar to the simulations for a single-cloud layer (Wang et al., 2008). Apparently, for optically thick absorbing aerosol layers in a cloud-free scene, the scene height gives the correct value of the aerosol layer height. The scene height and scene albedo seem more robust for the aerosol cases with large AOT. This is because by using Eq. (2), there is no contribution from the fixed surface albedo and cloud albedo, which do contribute to R_{sim} in Eq. (1). Therefore, in order to simulate large absorption or small R_{sim}, Eq. (2) will perform better than Eq. (1). This also explains the better behaviour of the scene albedo and scene pressure than that of the effective cloud fraction and cloud height for the optically thick aerosol cases. However, for optically thin aerosol cases the scene height is often lower than the aerosol layer height because the scene height is a radiance-weighted average of the surface height and aerosol layer height.

ACPD
11, 32685–32721, 2011

The results of the simulations for the cloudy cases are shown in Fig. 2. As shown in Fig. 2a, cloud height is not retrieved correctly for the case with AOT = 3.65 and SSA = 0.6, which is similar to the corresponding clear-sky case in Fig. 1a. In this case almost all light is absorbed by the aerosol layer, and although the clouds could serve as a bright surface, the reflectance remains too low. The aerosol case with AOT = 3.65 and SSA = 0.8 is brighter in the cloudy scene than in the clear-sky scene, so the FRESCO retrieval works. The retrieved cloud heights are mostly above the aerosol layer and increase for large SZA. The scene heights are lower than the retrieved cloud heights with the lowest height at 6 km, see Fig. 2b. Actually, for the AOT = 3.65 and SSA = 0.6, 0.8 cases, the retrieved cloud heights and scene heights are both close to the aerosol layer height. For the cases with AOT = 0.5 and SSA = 0.6, 0.8, the retrieved cloud heights and scene heights are close to the cloud layer at 1–2 km, because the AOT is too small as compared to the cloud optical thickness.

As illustrated in Fig. 2c and d, cloudy cases with AOT = 0.5, SSA = 0.6, 0.8 have larger effective cloud fractions and scene albedos than the corresponding clear-sky cases, because the cloud layer reflects more light back to the top of the atmosphere. The effective cloud fractions and scene albedos decrease with SZA, which is quite different from the behaviour for cloud-only scenes (not shown). We would expect that clouds are brighter at large SZA and that the effective cloud fractions and scene albedos increase with the SZA (so-called limb brightening). However, with absorbing aerosols above the clouds, at larger SZA the absorption by aerosols is stronger due to the longer light paths, so the increase of reflectance due to the longer scattering light paths is compromised (so-called limb darkening). For the cloudy cases with AOT = 3.65, SSA = 0.6, 0.8, the effective cloud fractions and scene albedos are only slightly increased compared to the corresponding clear-sky cases.

In summary, according to the above simulations the FRESCO cloud height and scene height may be interpreted as aerosol height for optically thick absorbing aerosols (e.g. AOT = 3.65, SSA = 0.6, 0.8) in clear-sky or cloudy situations. The scene height seems more robust for extremely absorbing aerosol cases (SSA = 0.6) than the cloud

ACPD
11, 32685–32721, 2011

height. For optically thin aerosol cases (AOT = 0.5, SSA = 0.6, 0.8), the FRESCO cloud height and scene height are close to the cloud layer height. The effective cloud fraction may become around 0.1 for optically thick aerosols (AOT = 3.65), which could be wrongly interpreted as thin clouds.

4 GOME-2 FRESCO results for absorbing aerosol events

Based on the simulations of Sect. 3, we would expect that the FRESCO cloud algorithm is able to retrieve reasonable aerosol heights, although the results will depend on the scenes. For scenes without clouds, FRESCO effective cloud fraction, cloud pressure, scene albedo, and scene pressure are actually corresponding aerosol parameters. The scene pressure will be most reliable for optically thick aerosol plumes. For cloudy scenes, the four FRESCO retrieved properties are a mixture of cloud and aerosol properties. In the following analysis we will show some examples of strongly absorbing aerosol events for clear-sky and cloudy scenes.

4.1 Volcanic ash plumes

GOME-2 captured the ash plume from the eruption of the Chilean volcano called Puyehue-Cordón Caulle (elevation 2236 m, 40.59° S, 72.12° W) firstly on 5 June 2011 and continued observations for several days. Figure 3 shows the MODIS RGB image, GOME-2 AAI and GOME-2 cloud images of 5 June 2011. The volcanic ash was injected at a high altitude and then transported to the east. According to the MODIS RGB image, the ash plume is in a cloud-free region over land and above the clouds over the ocean. The plume can be clearly identified in the AAI image. In the FRESCO cloud pressure and scene pressure images the plume is clearly visible as a high cloud. According to the FRESCO cloud pressure, the volcanic plume is at 200 hPa (12 km), which is higher than the surrounding clouds. The maximum AAI value is about 8. The plume cannot be distinguished from clouds in the FRESCO effective cloud fraction and

ACPD
11, 32685–32721, 2011

scene albedo maps, because the aerosol plume produces similar reflectances as the clouds nearby.

Figure 4 shows the scatter plots of the retrieved cloud information versus AAI for the pixels in the region of [35, 47]° S and [50, 70]° W, which is marked with a box in Fig. 3. Some cloud pressure values are comparable to the scene pressure values because the effective cloud fractions are close to 1. As shown in Fig. 4, the cloud pressure and scene pressure both decrease with the increasing AAI, whereas the effective cloud fraction and scene albedo both increase with increasing AAI. Therefore, the effective cloud fraction and scene albedo both follow the AAI sensitivity to aerosol presence. In aerosol-free cases over the dark ocean the effective cloud fraction and scene albedo are determined by the cloud optical thickness and geometric cloud fraction. In this case, the effective cloud fraction and scene albedo are determined by both clouds and aerosols.

The variation in AAI values of the selected aerosol plume as shown in Fig. 4 mainly depends on the height of the plume and the aerosol optical thickness, since the aerosol type and single scattering albedo values are probably very similar in the selected region of the plume. All the pixels in the plume are measured by GOME-2 within a few minutes; the variation in the solar zenith angle is small. The larger AAI values are corresponding to optically thick parts of the plume with large effective cloud fractions and a large plume height. As shown in Fig. 4a and c, some pixels have small AAI values, small effective cloud fraction values and large cloud pressures. This suggests that these parts of the plume are not optically thick, so that light can penetrate the aerosol layer and the retrieved plume heights are close to the clouds or the surface beneath. This behaviour agrees with the simulations for the thin aerosol cases (see Figs. 1 and 2).

On 6 June 2011, the Puyehue volcanic ash plumes show up in the GOME-2 AAI image in three orbits (see Fig. 5). In contrast to Fig. 3, the plumes also appear in the effective cloud fraction and scene albedo images; this is because the plumes are optically thicker than the surrounding clouds. The MODIS image shows the left plume (plume in the left orbit, over land and close to the volcano). The left plume first went to

ACPD
11, 32685–32721, 2011

the northeast, then turned to the southeast, forming a curl. The effective cloud fraction for the left plume is about 1. Inside the curl the aerosols are thinner because the surface is visible in the MODIS image and the FRESCO effective cloud fraction is about 0.3. In the FRESCO cloud images the thin aerosol plumes show up as having small effective cloud fractions, small scene albedos, high cloud pressures and high scene pressures; while the thick aerosol plumes result in large effective cloud fractions, large scene albedos, low cloud pressures and low scene pressures.

In the scatter plots for the left plume (see Fig. 6), the cloud pressures and scene pressures appear as two clusters, one at about 200 hPa and the other at 600–800 hPa. The left plume is mainly in a clear-sky region and the relation between the effective cloud fraction and the AAI is dominated by aerosols. The effective cloud fraction and scene albedo versus AAI plots have less scatter than in Fig. 4c and d and have less pixels with small AAI and large effective cloud fractions or scene albedos. This indicates that the pixels with small AAI and large effective cloud fractions are cloudy pixels. Figure 7 shows the scatter plots for the right side plume (along 30° W over the ocean). The plume is transported to the east at about 200 hPa, while the effective cloud fraction only ranges up to 0.4, which points to optically thinner aerosols and clouds. The AAI values for this right plume go up to 6, as compared to 8 for the left plume. Since these two plumes are at similar altitude, the AAI values should be similar if they would have similar optical thicknesses. The left plume has larger AAI values, which is probably due to larger aerosol optical thicknesses or smaller single scattering albedos (i.e. more absorption). Because the effective cloud fractions in the left plume are 2 times larger than those in the right plume, the AAI difference between the two plumes is more likely caused by the aerosol optical thickness than by the single scattering albedo. The right plume has been exposed to air longer than the plume close to the volcano; therefore it is more diluted by mixing with surrounding air or by deposition during the long range transport. The aerosol particles can also take up water vapour. Thus, the absorption of the aerosols is reduced, which also leads to smaller AAI values of the aerosol plume.

ACPD
11, 32685–32721, 2011

In summary, the eruption of the Puyehue volcano in Chile in June 2011 produced a nice example for our analysis. The volcanic ash plume is optically thick and its height is much higher than the clouds below it. If the plume would have been close to the surface or optically thinner, the plume shape might not be so easily identified in the FRESCO cloud images. It shows that the FRESCO cloud pressure and scene pressure indicate the aerosol layer pressure for these volcanic plumes, especially for pixels with large AAI values. For pixels with small AAI values, the large effective cloud fractions and associated pressures are most probably caused by clouds. Scene pressure is a more robust quantity than cloud pressure, because it shows less scatter.

4.2 Saharan desert dust

The Western Sahara is a main source of dust and mineral aerosols (Kaufman et al., 2005). The Saharan dust storms, which peak in June/July, are controlled by small-scale high-wind events (De Graaf et al., 2005; Engelstaedter and Washington, 2007). We selected an event on 30 June 2010 based on GOME-2 AAI images and MODIS images.

Figure 8 shows the MODIS Terra image over the Sahara desert measured at 10:30–10:35 UTC on 30 June 2010 and the GOME-2 AAI and FRESCO cloud images. The dust plume is clearly visible over the Sahara desert around 20° N and 0–10° E. There are only a few scattered clouds in the dust storm area. The dust plume as seen in the GOME-2 AAI image is associated with high AAI values up to 6. The FRESCO effective cloud fraction image is in agreement with the MODIS image. For the areas with large AAI values, the effective cloud fractions are up to 0.3. Because we selected largely cloud-free areas, the FRESCO cloud parameters can be regarded as aerosol parameters.

The scatter plots between FRESCO cloud results and AAI for the area of the dust plume between [20, 26]° N, [−5, 10]° E are shown in Fig. 9. It appears that most cloud pressures are higher than 500 hPa and most scene pressures are higher than 800 hPa. For pixels with AAI < 4, some cloud and scene pressure values are close to 1000 hPa,

ACPD
11, 32685–32721, 2011

probably because the cloud or aerosol layers are quite thin. The aerosols with AAI > 4 are mainly at 850–900 hPa. In the cloud pressure and scene pressure versus AAI plots, the cloud pressures tend to increase with AAI; the heights of the dust plumes are lower at large AAI. This suggests that the optically thick aerosols are close to the surface. The dust plumes are generated at the surface; therefore, it is quite reasonable that the dust plumes are optically thicker at lower altitude in the source region. Please note the contrast with the volcanic ash plumes (shown in Figs. 4 and 7) which tops are at similar heights, and have no significant decrease at large AAI. This is because the volcanic ash plumes are produced from a point source and are generally transported at a similar altitude above the surface.

The effective cloud fractions of the Saharan dust plumes increase with AAI (see Fig. 9), which indicates that the effective cloud fraction contains aerosol optical thickness information. The cloud pressure and scene pressure show no clear correlation with AAI. Therefore, the variability of AAI for this dust plume event is due to the sensitivity of the AAI to aerosol optical thickness but not to aerosol height.

Because the selected dust plume area is mainly cloud-free, the scene albedo is a mixture of surface albedo and aerosol plume albedo. Since the surface albedo at the FRESCO wavelengths around 760 nm is large in the desert, the scene albedo may have a large contribution from the surface. The mean surface albedo around 760 nm in this area is 0.40, with a minimum surface albedo of 0.2. Therefore, in Fig. 9 the scene albedo is larger than 0.2, even if the cloud fraction is 0.

4.3 Biomass burning aerosols

Biomass burning aerosol is absorbing in the UV and can be detected by the AAI. We will present a biomass burning aerosol case in south west Africa on 6 August 2010. In Fig. 10, the MODIS fire count map at 09:20 UTC on 6 August shows the fires as red spots. The smoke is caused by biomass burning on land and is transported westwards to the ocean above the marine stratocumulus cloud fields at about 900 hPa (see Fig. 10). Between [10, 20]° S the GOME-2 AAI map shows a sharp boundary

ACPD
11, 32685–32721, 2011

between land and ocean. The high AAI values are mainly over ocean in this region. The smoke over land in the cloud-free region may not be detected due to the relatively small aerosol optical thickness and the low surface albedo. Over ocean, the AAI is enhanced due to the reflection from the bright stratocumulus clouds below the smoke. As illustrated in Fig. 10, the FRESCO effective cloud fraction and scene albedo maps are in good agreement with the MODIS image and the AAI map. The northeast part of the smoke plume is in a cloud-free region over land and shows small effective cloud fraction values. The cloud pressure map is quite homogeneous for the smoke area. The low pressures at about 130 hPa at [15, 20]° S next to the smoke area seem to be unrealistic, because there are almost no clouds or aerosols and the cloud fraction is very low. This artefact in the retrieved cloud pressure is a result of the low level of reflected light. However, for the same region, the scene pressure is retrieved correctly, namely close to the surface.

The scatter plots of Fig. 11 show the FRESCO cloud data versus the AAI data from GOME-2 measurements in the area of [5, 15]° S and [10, 15]° E. Figure 11c and d show that the effective cloud fraction and scene albedo both increase with the increasing AAI. This suggests that the effective cloud fractions are related to both cloud and aerosol optical thickness. The relatively large effective cloud fraction is mainly due to the clouds. For low altitude aerosols in cloud-free scenes (cf. the desert dust case in Fig. 9), an AAI value of 5 means an effective cloud fraction of about 0.3. For smoke over clouds with similar AAI values, the effective cloud fraction reaches about 0.6–0.8, clearly due to the contribution from the cloud layer. Similarly, the scene albedo has contributions from clouds and aerosols, but it is mainly the bright cloud layer that leads to the large scene albedo values.

The FRESCO cloud pressures and scene pressures are comparable due to the large effective cloud fractions (see Fig. 11a and b). The smoke plume seems quite thin in the MODIS image. According to our simulations in Sect. 3 the FRESCO cloud pressure and scene pressure are then close to the cloud layer pressure (see Fig. 2). This result agrees with the findings reported by Waquet et al. (2009), who analysed the aerosol

ACPD
11, 32685–32721, 2011

and cloud heights from A-Train observations for a similar biomass burning aerosol case over low-level clouds over ocean. According to their case study, the Cloud Aerosol Lidar with Orthogonal Polarization (CALIOP) measured the aerosol layer to be located between 3 and 4 km and the cloud top height to be at about 1 km. The aerosol optical thickness of 0.225 (at 865 nm) was derived from the Polarization and Anisotropy of Reflectances for Atmospheric Sciences coupled with Observations from a Lidar (PARASOL) measurement. The cloud height retrieved from O_2 A band measurements agreed well with the cloud height measured by CALIOP.

4.4 Smoke from Russian wild fires

The smoke from wild fires in Russia in August 2010 clearly shows up in the GOME-2 AAI maps and MODIS fire count map of 1 August 2010 (see Fig. 12). The smoke plume takes the form of an "S" shape in the MODIS image, right above the fire sources (red spots in the image). Based on the MODIS image, the smoke seems to be located above the clouds; for some places the surface is visible in the cloud-free area. The MODIS image shows more clouds in the northern part of the plume than in the southern part. The shape of the plume appears to be the same in the AAI image as in the effective cloud fraction image. The cloud pressures are lower in the northern part (60° N) and higher in the southern part of the plume (around 55° N). However, it is difficult to distinguish the smoke pressure in the FRESCO cloud pressure and scene pressure maps. The maximum AAI value reached is 6 for this plume. According to Witte et al. (2011), SSA values of 0.92 were observed during the wild fire period and the aerosol optical thickness was about 1 on 1 August 2010.

The scatter plots of the FRESCO cloud products versus AAI in the area of [52, 60]° N and [35, 56]° E are shown in Fig. 13. The cloud pressure increases with AAI which indicates that the thickest plume is located at the lowest altitude. This is similar to the case of the dust plume in the Sahara desert. Here, the thickest smoke is measured close to the source of the fires. The cloud pressure and scene pressure values mostly vary between 400 hPa and the surface, which indicates the variation of the smoke

ACPD
11, 32685–32721, 2011

plume height. The effective cloud fraction and scene albedo both increase with AAI, which stresses the sensitivity of AAI to aerosol optical thickness, and shows that the FRESCO cloud product contains information about the smoke. The averaged surface albedo for this area is 0.255; therefore the smallest scene albedo is about 0.3 because of the contribution of clouds and/or aerosols. The cloud pressure and scene pressure contain information on aerosol pressure. However, it is difficult to tell whether the cloud pressure is close to the aerosol layer or close to the cloud layer. Since the smoke with the large AAI values should be above the clouds (otherwise the aerosols would not be visible), the cloud pressure or scene pressure can be used as a lower boundary of the aerosol height.

5 Conclusions

We have analysed GOME-2 FRESCO cloud retrievals for absorbing aerosol events. We first demonstrated with simulated FRESCO data that the FRESCO algorithm can retrieve aerosol height for optically thick aerosol cases. Next we presented four typical events with strongly absorbing aerosols: the Puyehue volcanic ash plume, a Saharan desert dust event, an African biomass burning smoke event, and a Russian wild fire smoke event. The analysis was based on the sensitivity of the Absorbing Aerosol Index (AAI) to the aerosol optical thickness and aerosol layer height. If the AAI sensitivity is observed from the correlation of FRESCO cloud retrievals with the AAI, the FRESCO cloud retrievals contain aerosol information.

For the four events, effective cloud fraction and scene albedo both increase with AAI, resulting from the sensitivity of AAI to aerosol optical thickness. The FRESCO effective cloud fraction and scene albedo contain aerosol optical thickness information. If the pixel is cloud-free, the effective cloud fraction takes up the role of effective aerosol fraction and the scene albedo is a mixture of the aerosol layer albedo and the surface albedo. The effective cloud fraction cannot be interpreted as cloud or aerosol optical thickness directly, but the correlation of effective cloud fraction and AAI indicates that aerosol information is present in the O_2 A band measurements.

ACPD
11, 32685–32721, 2011

The FRESCO cloud pressure and scene pressure are more relevant quantities than the effective cloud fraction and scene albedo, because they give important information for aviation safety, in addition to the AAI. For optically thick and strongly absorbing aerosols, the FRESCO cloud height is actually the aerosol height, especially when the aerosols are above the cloud layer and can be distinguished from its surroundings. In clear-sky situations, the FRESCO cloud height can be interpreted as aerosol height. For optically thin aerosols, the retrieved aerosol height may be at the surface. For optically thin aerosol layers above thick clouds, the retrieved height is close to the cloud height. For aerosol plumes close to the source, the cloud height decreases with increasing AAI, for example in the case of the Russian wild fire smoke event and the Saharan desert dust event. If the aerosol plume is transported away from the source, the plume height usually does not decrease with AAI but stays at a constant level, for example in the studied cases of volcanic ash plumes and the biomass burning smoke over stratocumulus clouds.

According to our simulations, the scene pressure seems to be more robust for the determination of aerosol height than the cloud pressure for extremely absorbing aerosol cases. In the events we analysed here there were no extremely absorbing aerosol cases; the maximum AAI occurring was 8. If, in the case of an aerosol plume, the cloud pressure shows a completely different behaviour than the scene pressure, and the AAI values are very large, then the scene pressure is likely more reliable than the cloud pressure. In this case, the effective cloud fraction should be close to 0 or slightly negative, which is also a feature of extremely absorbing aerosol cases.

Although the FRESCO algorithm is designed for clouds, for optically thick aerosols the effective cloud fraction and cloud height could be regarded as the effective aerosol fraction and aerosol height. When using the FRESCO cloud product, this feature has to be taken into account. The cloud pressure and scene pressure can potentially provide useful aerosol height information, but the interpretation should be also based on AAI and cloud images.

ACPD
11, 32685–32721, 2011

Acknowledgements. We would like to thank Reinout Boers (KNMI) for helpful comments and suggestions on the manuscript. This work was supported by Netherlands Space Office as part of the SCIA-Visie project. We would like to acknowledge EUMETSAT and the O3M SAF for GOME-2 data processing and data provision. The MODIS team is acknowledged for providing the MODIS images. The MODIS RGB images were downloaded from LAADS Web (http://ladsweb.nascom.nasa.gov/browse_images/). The MODIS fire count maps were downloaded from the MODIS Rapid Response System http://rapidfire.sci.gsfc.nasa.gov/. The FRESCO and AAI data are available from the TEMIS website http://www.temis.nl.

References

Anderson, G. P., Clough, S. A., Kneizys, F. X., Chetwynd, J. H., and Shettle, E. P.: AFGL atmospheric constituent profiles, Tech. Rep. AFGL-TR-86-0110, Air Force Geophys. Lab., Hanscom AFB, Mass, 1986. 32690

Boesche, E., Stammes, P., and Bennartz, R.: Aerosol influence on polarization and intensity in near-Infrared O_2 and CO_2 absorption bands observed from space, J. Quant. Spectrosc. Ra., 110, 3, 223–239, doi:10.1016/j.jqsrt.2008.09.019, 2009. 32687

Bovensmann, H., Burrows, J. P., Buchwitz, M., Frerick, J., Noël, S., Rozanov, V. V., Chance, K. V., and Goede, A. H. P.: SCIAMACHY – Mission objectives and measurement modes, J. Atmos. Sci., 56, 127–150, 1999. 32686

De Graaf, M., Stammes, P., Torres, O., and Koelemeijer, R. B. A.: Absorbing Aerosol Index: Sensitivity analysis, application to GOME and comparison with TOMS, J. Geophys. Res., 110, D01201, doi:10.1029/2004JD005178, 2005. 32687, 32691, 32693, 32699

De Graaf, M., Tilstra, L. G., Aben, I., and Stammes, P.: Satellite observations of the seasonal cycles of absorbing aerosols in Africa related to the monsoon rainfall; 1995–2008, Atmos. Environ., 44, 1274–1283, doi:10.1016/j.atmosenv.2009.12.038, 2010a. 32688

De Graaf, M., Tuinder, O., and Tilstra, L. G.: O3MSAF Algorithm Theoretical Basis Document for ARS, O3MSAF/KNMI/ATBD/002, http://o3msaf.fmi.fi/docs/atbd/Algorithm_Theoretical_Basis_Document_ARS_Apr_2010.pdf, 2010b. 32691

De Haan, J. F., Bosma, P. B., and Hovenier, J. W.: The adding method for multiple scattering calculations of polarized light, Astron. Astrophys., 183, 371–391, 1987. 32693

Dirksen, R. J., Boersma, K. F., de Laat, J., Stammes, P., van der Werf, G. R., Val Martin, M., and

ACPD

11, 32685–32721, 2011

Kelder, H. M.: An aerosol boomerang: Rapid around-the-world transport of smoke from the December 2006 Australian forest fires observed from space, J. Geophys. Res., 114, D21201, doi:10.1029/2009JD012360, 2009. 32688
Dubuisson, P., Frouin, R., Dessailly, D., Duforêt, L., Léon, J.-F., Voss, K., and Antoine, D.: Estimating the altitude of aerosol plumes over the ocean from reflectance ratio measurements in the O_2 A-band, Remote Sens. Environ., 113, 1899–1911, 2009. 32687
Eckardt, F. D. and Kuring, N.: SeaWiFS identifies dust sources in the Namib Desert, Int. J. Remote Sens., 26, 4159–4167, doi:10.1080/01431160500113112, 2005. 32688
Engelstaedter, S. and Washington, R.: Atmospheric controls on the annual cycle of North African dust, J. Geophys. Res., 112, D03103, doi:10.1029/2006JD007195, 2007. 32699
Fromm, M., Tupper, A., Rosenfeld, D., Servranckx, R., and McRae, R.: Violent pyroconvective storm devastates Australia's capital and pollutes the stratosphere, Geophys. Res. Lett., 33, L05815, doi:10.1029/2005GL025161, 2006. 32688
Grzegorski, M., Wenig, M., Platt, U., Stammes, P., Fournier, N., and Wagner, T.: The Heidelberg iterative cloud retrieval utilities (HICRU) and its application to GOME data, Atmos. Chem. Phys., 6, 4461–4476, doi:10.5194/acp-6-4461-2006, 2006. 32687
Guan, H., Esswein, R., Lopez, J., Bergstrom, R., Warnock, A., Follette-Cook, M., Fromm, M., and Iraci, L. T.: A multi-decadal history of biomass burning plume heights identified using aerosol index measurements, Atmos. Chem. Phys., 10, 6461–6469, doi:10.5194/acp-10-6461-2010, 2010. 32688
Johnson, B. T., Osborne, S. R., Haywood, J. M., and Harrison, M. A. J.: Aircraft measurements of biomass burning aerosol over West Africa during DABEX, J. Geophys. Res., 113, D00C06, doi:10.1029/2007JD009451, 2008. 32693
Jeong, M.-J. and Hsu, N. C.: Retrievals of aerosol single-scattering albedo and effective aerosol layer height for biomass-burning smoke: Synergy derived from A-Train sensors, Geophys. Res. Lett., 35, L24801, doi:10.1029/2008GL036279, 2008. 32691
Kaufman, Y. J., Koren, I., Remer, L. A., Tanré, D., Ginoux, P., and Fan, S.: Dust transport and deposition observed from the Terra-Moderate Resolution Imaging Spectroradiometer (MODIS) spacecraft over the Atlantic Ocean, J. Geophys. Res., 110, D10S12, doi:10.1029/2003JD004436, 2005. 32688, 32699
Koelemeijer, R. B. A., Stammes, P., Hovenier, J. W., and de Haan, J. F.: A fast method for retrieval of cloud parameters using oxygen A band measurements from GOME, J. Geophys. Res., 106, 3475–3490, 2001. 32687, 32690

ACPD
11, 32685–32721, 2011

Koelemeijer, R. B. A., de Haan, J. F., and Stammes, P.: A database of spectral surface reflectivity in the range 335–772 nm derived from 5.5 years of GOME observations, J. Geophys. Res., 108, D24070, doi:10.1029/2002JD002429, 2003. 32690

Kokhanovsky, A. A., Rozanov, V. V., Nauss, T., Reudenbach, C., Daniel, J. S., Miller, H. L., and Burrows, J. P.: The semianalytical cloud retrieval algorithm for SCIAMACHY I. The validation, Atmos. Chem. Phys., 6, 1905–1911, doi:10.5194/acp-6-1905-2006, 2006. 32687

Krijger, J. M., van Weele, M., Aben, I., and Frey, R.: Technical Note: The effect of sensor resolution on the number of cloud-free observations from space, Atmos. Chem. Phys., 7, 2881–2891, doi:10.5194/acp-7-2881-2007, 2007. 32690

Loyola, D.: Automatic cloud analysis from polar-orbiting satellites using neural network and data fusion techniques, in: Proceedings of the IEEE International Geoscience and Remote Sensing Symposium, IGARSS'2004, Anchorage, 4, 2530–2534, 2004. 32687

Munro, R., Eisinger, M., Anderson, C., Callies, J., Corpaccioli, E., Lang, R., Lefebvre, A., Livschitz, Y., and Albinana, A. P.: GOME-2 on MetOp, Proceeding of the 2006 EUMETSAT Meteorological Satellite Conference, Helsinki, Finland, 12–16 June 2006, EUMETSAT, p. 48, 2006. 32686, 32688

Popp, C., Wang, P., Brunner, D., Stammes, P., Zhou, Y., and Grzegorski, M.: MERIS albedo climatology for FRESCO+ O_2 A-band cloud retrieval, Atmos. Meas. Tech., 4, 463–483, doi:10.5194/amt-4-463-2011, 2011. 32690

Rothman, L. S., Gordon, I. E., Barbe, A., Benner, D. C., Bernath, P. F., Birk, M., Boudon, V., Brown, L. R., Campargue, A., Champion, J.-P., Chance, K., Coudert, L. H., Dana, V., Devi, V. M., Fally, S., Flaud, J.-M., Gamache, R. R., Goldman, A., Jacquemart, D., Kleiner, I., Lacome, N., Lafferty, W. J., Mandin, J.-Y., Massie, S. T., Mikhailenko, S. N., Miller, C. E., Moazzen-Ahmadi, N., Naumenko, O. V., Nikitin, A. V., Orphal, J., Perevalov, V. I., Perrin, A., Predoi-Cross, A., Rinsland, C. P., Rotger, M., Šimečková, M., Smith, M. A. H., Sung, K., Tashkun, S. A., Tennyson, J., Toth, R. A., Vandaele, A. C., Vander Auwera, J.: The HITRAN 2008 molecular spectroscopic database, J. Quant. Spectrosc. Ra., 110, 533–572, 2009. 32690

Stammes, P.: Spectral radiance modeling in the UV-visible range, in: IRS 2000: Current Problems in Atmospheric Radiation, edited by: Smith, W. and Timofeyev, Y., A. Deepak, Hampton, Va., 385–388, 2001. 32693

Stammes, P., Sneep, M., de Haan, J. F., Veefkind, J. P., Wang, P., and Levelt, P. F.: Effective cloud fractions from the Ozone Monitoring Instrument: Theoretical framework and validation,

ACPD
11, 32685–32721, 2011

J. Geophys. Res., 113, D16S38, doi:10.1029/2007JD008820, 2008. 32690
Tilstra, L. G., Tuinder, O. N. E., and Stammes, P.: GOME-2 Absorbing Aerosol Index: Statistical analysis, comparison to GOME-1 and impact of instrument degradation, in: Proceedings of the 2010 EUMETSAT Meteorological Satellite Conference, EUMETSAT, p. 57, ISBN 978-92-9110-089-7, 2010. 32687, 32691
Torres, O., Bhartia, P. K., Herman, J. R., Ahmad, Z., and Gleason, J.: Derivation of aerosol properties from satellite measurements of backscattered ultraviolet radiation: theoretical basis, J. Geophys. Res., 103, D14, doi:10.1029/98JD00900, 1998. 32687, 32691
Torres, O., Tanskanen, A., Veihelmann, B., Ahn, C., Braak, R., Bhartia, P. K., Veefkind, P., and Levelt, P.: Aerosols and surface UV products from Ozone Monitoring Instrument observations: an overview, J. Geophys. Res. 112, D24S47, doi:10.1029/2007JD008809, 2007. 32687
Wang, P. and Stammes, P.: FRESCO-GOME2 project, EUM/CO/06/1536/FM, final report, Eumetsat, Darmstadt, 14 September, 2007. 32688
Wang, P., Stammes, P., van der A, R., Pinardi, G., and van Roozendael, M.: FRESCO+: an improved O_2 A-band cloud retrieval algorithm for tropospheric trace gas retrievals, Atmos. Chem. Phys., 8, 6565–6576, doi:10.5194/acp-8-6565-2008, 2008. 32687, 32689, 32690, 32694
Wang, P. and van der A, R.: Product Specification Document FRESCO, TEM/PSD2/003, http://www.temis.nl/docs/PSD_FRESCO.pdf, 2011. 32690
Wang, P., Stammes, P., and Mueller, R.: Surface solar irradiance from SCIAMACHY measurements: algorithm and validation, Atmos. Meas. Tech., 4, 875–891, doi:10.5194/amt-4-875-2011, 2011. 32690
Waquet, F., Riedi, J., Labonnote, L. C., and Goloub, P.: Aerosol remote sensing over clouds using A-Train observations, J. Atmos. Sci., 66, 2468–2480, doi:10.1175/2009JAS3026.1, 2009. 32701
Witte, J. C., Douglass, A. R., da Silva, A., Torres, O., Levy, R., and Duncan, B. N.: NASA A-Train and Terra observations of the 2010 Russian wildfires, Atmos. Chem. Phys., 11, 9287–9301, doi:10.5194/acp-11-9287-2011, 2011. 32688, 32702

ACPD
11, 32685–32721, 2011

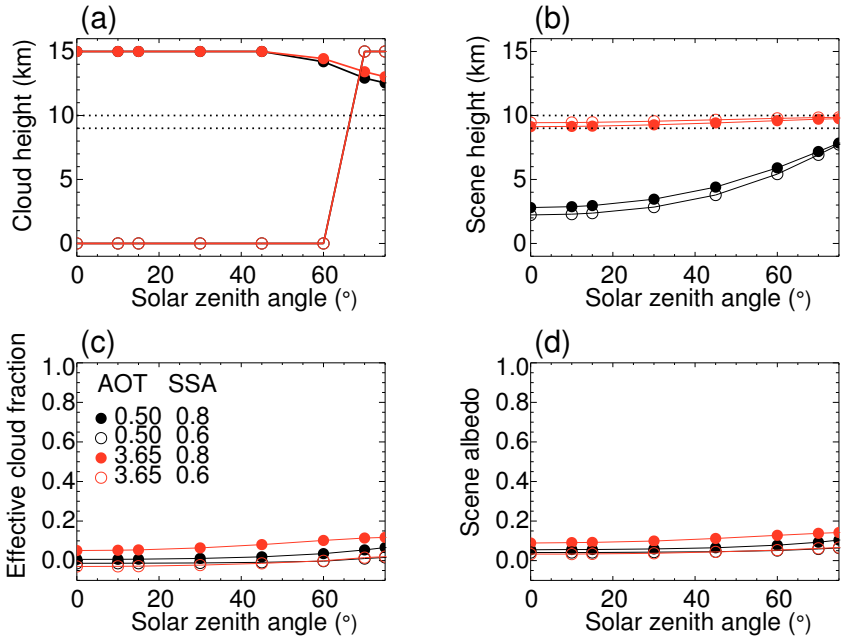

Fig. 1. FRESCO retrieval results of **(a)** cloud height, **(b)** scene height, **(c)** effective cloud fraction, and **(d)** scene albedo using simulated O_2 A band spectra for aerosols in a clear-sky scene (COT = 0). Surface albedo is 0.05. Aerosol asymmetry parameter is 0.7. Aerosol optical thickness (AOT) is 0.5 and 3.65, respectively. The aerosol single scattering albedo (SSA) values are 0.6 and 0.8. The aerosol layer is located between 9 and 10 km, indicated with black dashed lines. Viewing direction is nadir.

ACPD
11, 32685–32721, 2011

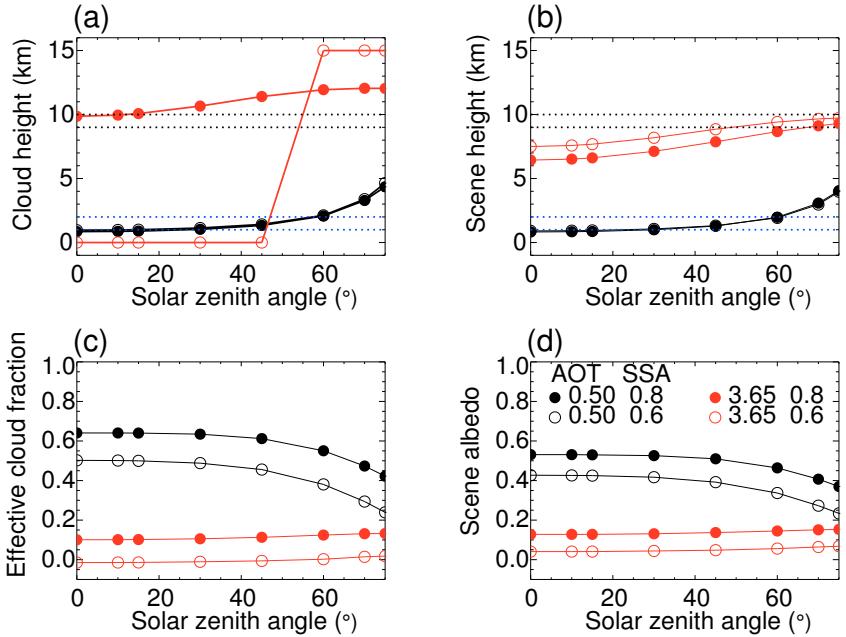

Fig. 2. FRESCO retrieval results of **(a)** cloud height, **(b)** scene height, **(c)** effective cloud fraction, and **(d)** scene albedo using simulated O_2 A band spectra for aerosols in cloudy scenes (COT = 20). The cloud layer is located between 1 and 2 km, noted with blue dashed lines and the location of aerosol layer is at 9–10 km, indicated with black dashed lines. Surface albedo is 0.05. Aerosol asymmetry parameter is 0.7. Aerosol optical thickness (AOT) is 0.5 and 3.65. The aerosol single scattering albedo (SSA) values are 0.6 and 0.8. Cloud particle asymmetry parameter is 0.85 and cloud single scattering albedo is 1. Viewing direction is nadir.

ACPD
11, 32685–32721, 2011

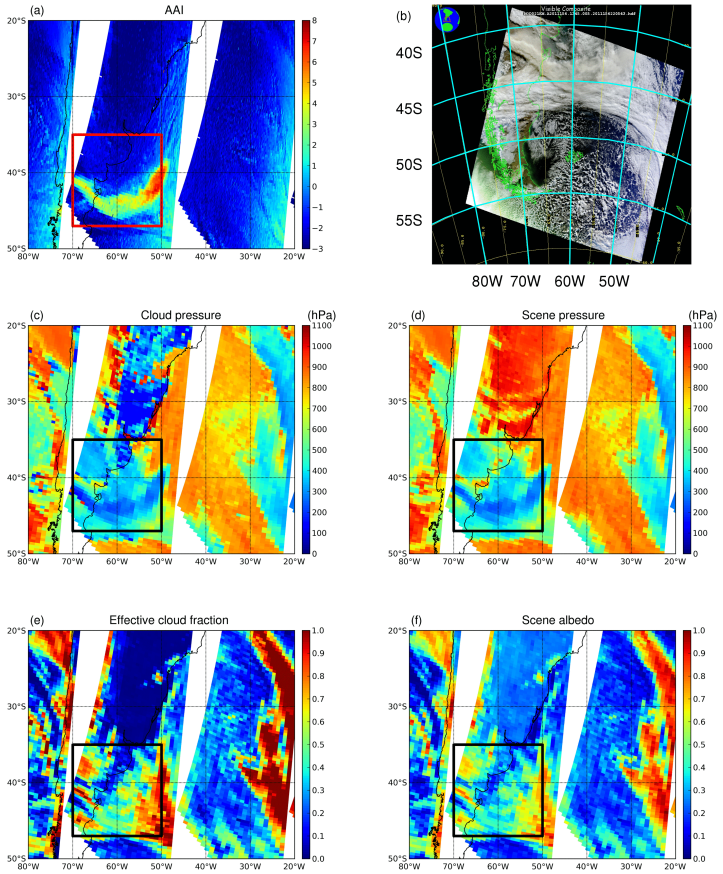

Fig. 3. **(a)** GOME-2 AAI image, **(b)** MODIS RGB image, **(c)** GOME-2 cloud pressure, **(d)** GOME-2 scene pressure, **(e)** GOME-2 effective cloud fraction, and **(f)** GOME-2 scene albedo for the Puyehue volcanic ash plume on 5 June 2011. The location of the plume is indicated with a box in the GOME-2 images. The plume in the box was measured around 12:50 UTC. MODIS image was measured at 13:45 UTC and was downloaded from LAADS Web (http://ladsweb.nascom.nasa.gov/browse_images/).

ACPD
11, 32685–32721, 2011

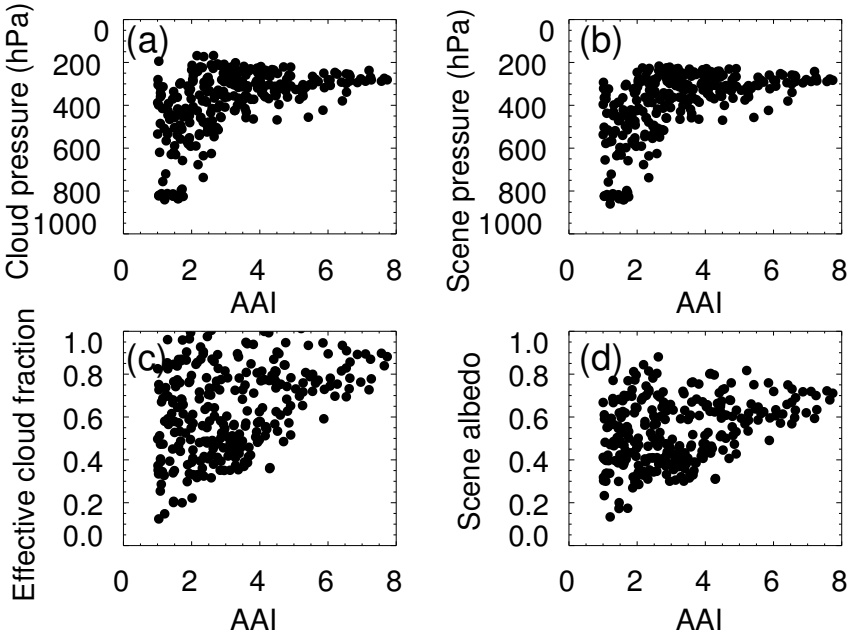

Fig. 4. Scatter plots of FRESCO **(a)** cloud pressure, **(b)** scene pressure, **(c)** effective cloud fraction, and **(d)** scene albedo versus absorbing aerosol index (AAI) from GOME-2 measurements of the Puyehue volcanic ash plume on 5 June 2011 around 12:50 UTC. The pixels used in the scatter plots are marked with a box in Fig. 3 in the region of [35, 47]° S and [50, 70]° W.

ACPD
11, 32685–32721, 2011

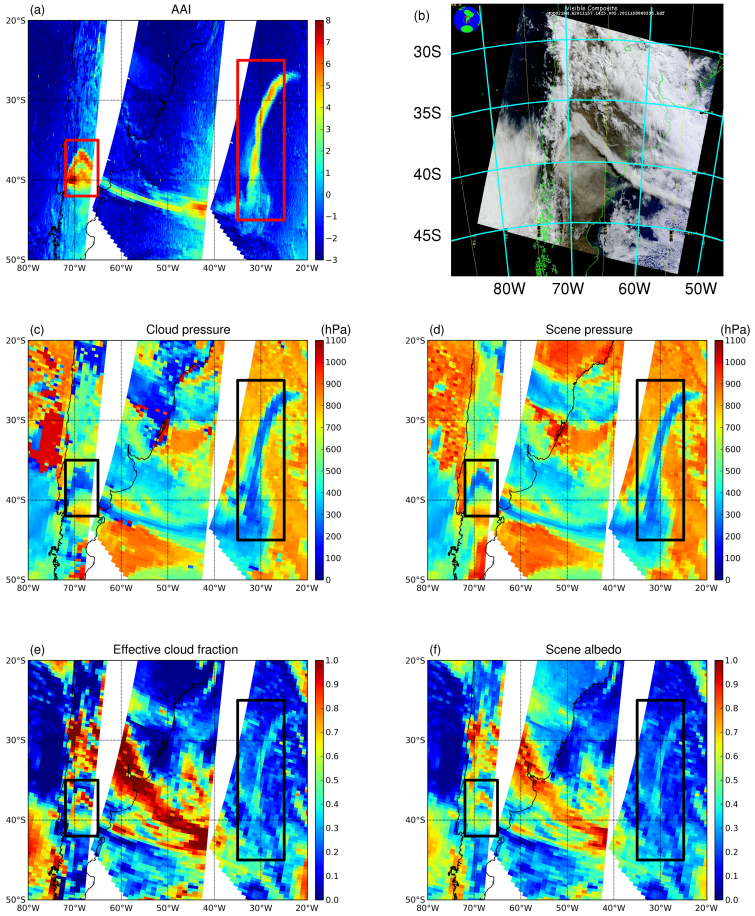

Fig. 5. **(a)** GOME-2 AAI image, **(b)** MODIS RGB image, **(c)** GOME-2 cloud pressure, **(d)** GOME-2 scene pressure, **(e)** GOME-2 effective cloud fraction, and **(f)** GOME-2 scene albedo for the Puyehue volcanic ash plume on 6 June 2011. The location of the plume is indicated with a box in the GOME-2 images. The plumes in the left and right boxes were measured around 14:10 and 10:45 UTC, respectively. The MODIS image was measured at 14:25 UTC.

ACPD
11, 32685–32721, 2011

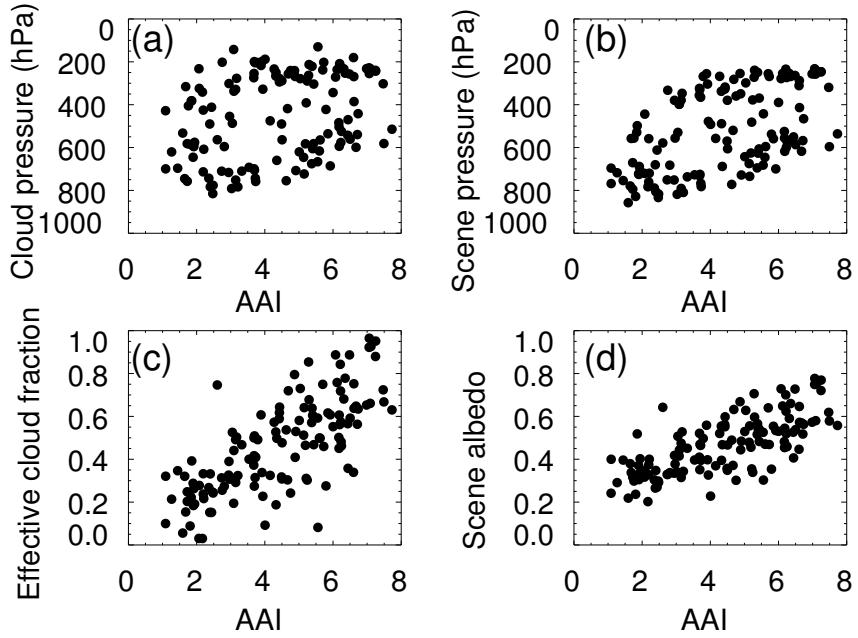

Fig. 6. Scatter plots of FRESCO **(a)** cloud pressure, **(b)** scene pressure, **(c)** effective cloud fraction, and **(d)** scene albedo versus absorbing aerosol index (AAI) from GOME-2 measurements of the Puyehue volcanic ash plume on 6 June 2011 around 14:10 UTC. The pixels used in the scatter plots are marked with the left box in Fig. 5 in the region of [35, 42]° S and [65, 72]° W.

ACPD
11, 32685–32721, 2011

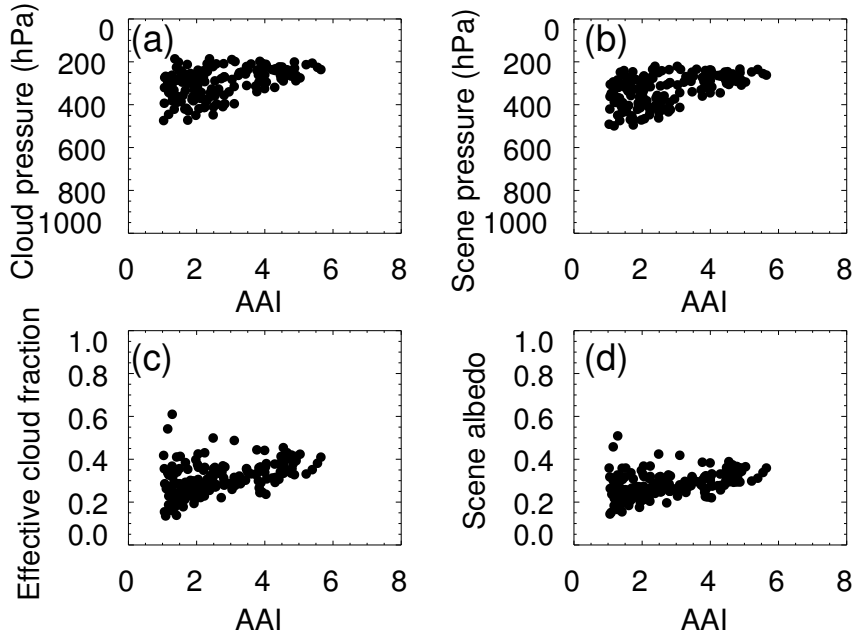

Fig. 7. Scatter plots of FRESCO **(a)** cloud pressure, **(b)** scene pressure, **(c)** effective cloud fraction, and **(d)** scene albedo versus absorbing aerosol index (AAI) from GOME-2 measurements of the Puyehue volcanic ash plume on 6 June 2011 around 10:45 UTC. The pixels used in the scatter plots are marked with the right box in Fig. 5 in the region of [25, 45]° S and [25, 35]° W.

ACPD
11, 32685–32721, 2011

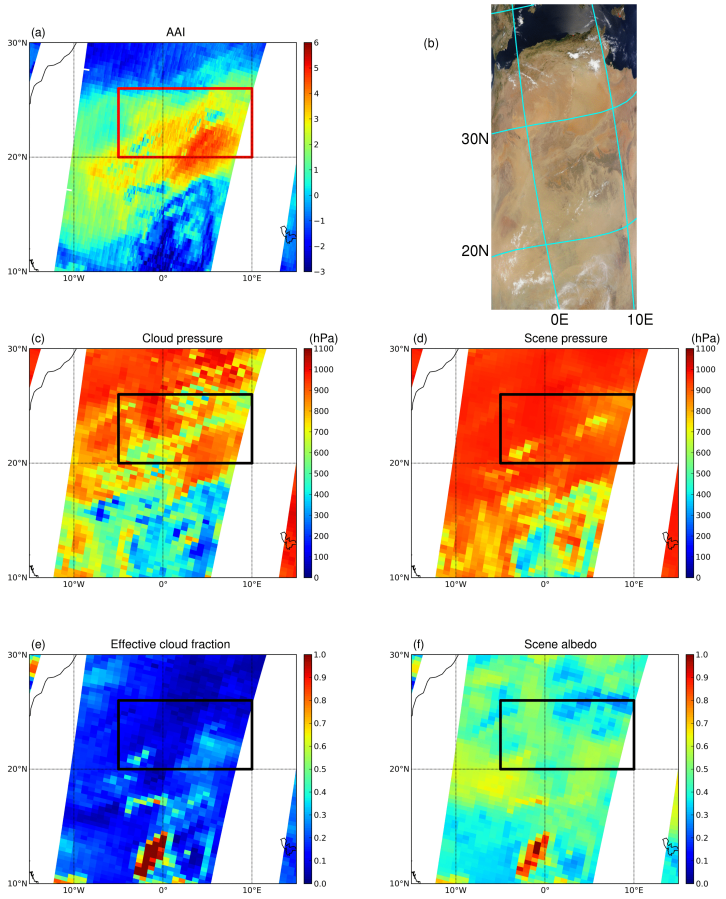

Fig. 8. **(a)** GOME-2 AAI image, **(b)** MODIS RGB image, **(c)** GOME-2 cloud pressure, **(d)** GOME-2 scene pressure, **(e)** GOME-2 effective cloud fraction, and **(f)** GOME-2 scene albedo for the Saharan desert dust event on 30 June 2010. The location of the plume is indicated with a box in the GOME-2 images. The plume in the box was measured around 09:45 UTC. The MODIS image was measured at 10:30 UTC. The MODIS image is downloaded from the MODIS Rapid Response System (http://rapidfire.sci.gsfc.nasa.gov/).

ACPD
11, 32685–32721, 2011

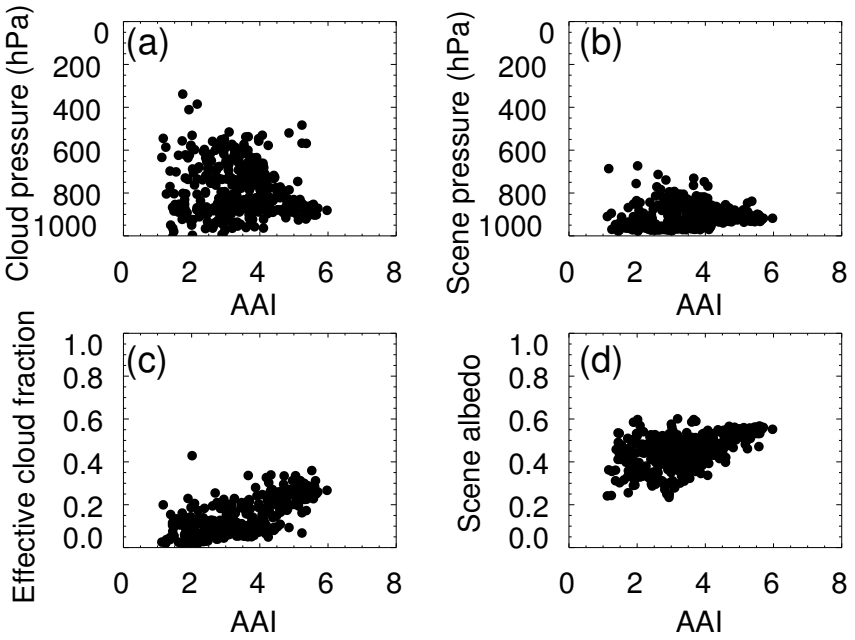

Fig. 9. Scatter plots of FRESCO **(a)** cloud pressure, **(b)** scene pressure, **(c)** effective cloud fraction, and **(d)** scene albedo versus absorbing aerosol index (AAI) from GOME-2 measurements of the Saharan desert dust event on 30 June 2010 around 09:45 UTC. The pixels used in the scatter plots are marked with a box in Fig. 8 in the region of [20, 26]° N and [−5, 10]° E.

ACPD
11, 32685–32721, 2011

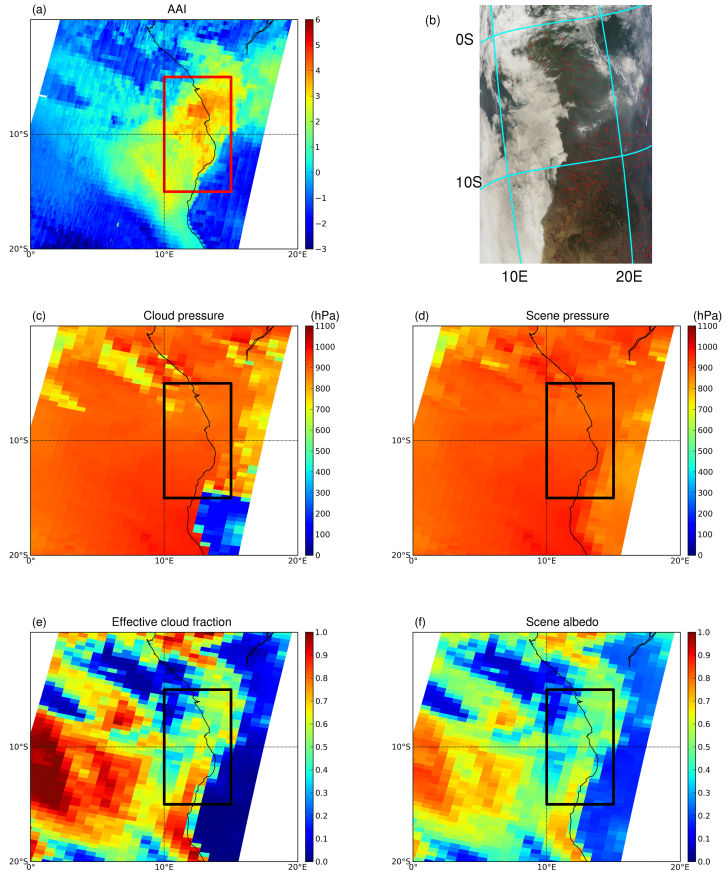

Fig. 10. **(a)** GOME-2 AAI image, **(b)** MODIS RGB image, **(c)** GOME-2 cloud pressure, **(d)** GOME-2 scene pressure, **(e)** GOME-2 effective cloud fraction, and **(f)** GOME-2 scene albedo for the biomass burning smoke event in West Africa on 6 August 2010. The location of the plume is indicated with a box in the GOME-2 images. The plume in the box was measured around 08:48 UTC. MODIS image was measured at 09:20 UTC. The red spots in MODIS images indicate fires.

ACPD
11, 32685–32721, 2011

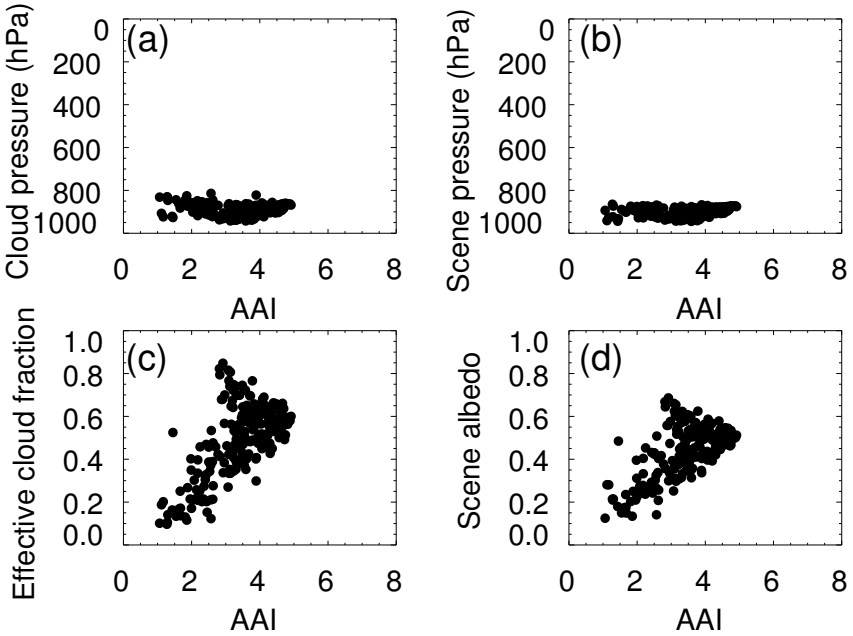

Fig. 11. Scatter plots of FRESCO **(a)** cloud pressure, **(b)** scene pressure, **(c)** effective cloud fraction, and **(d)** scene albedo versus absorbing aerosol index (AAI) from GOME-2 measurements of the biomass burning smoke event in West Africa on 6 August 2010 around 08:48 UTC. The pixels used in the scatter plots are marked with a box in Fig. 10 in the region of and [5, 15]° S and [10, 15]° E.

ACPD
11, 32685–32721, 2011

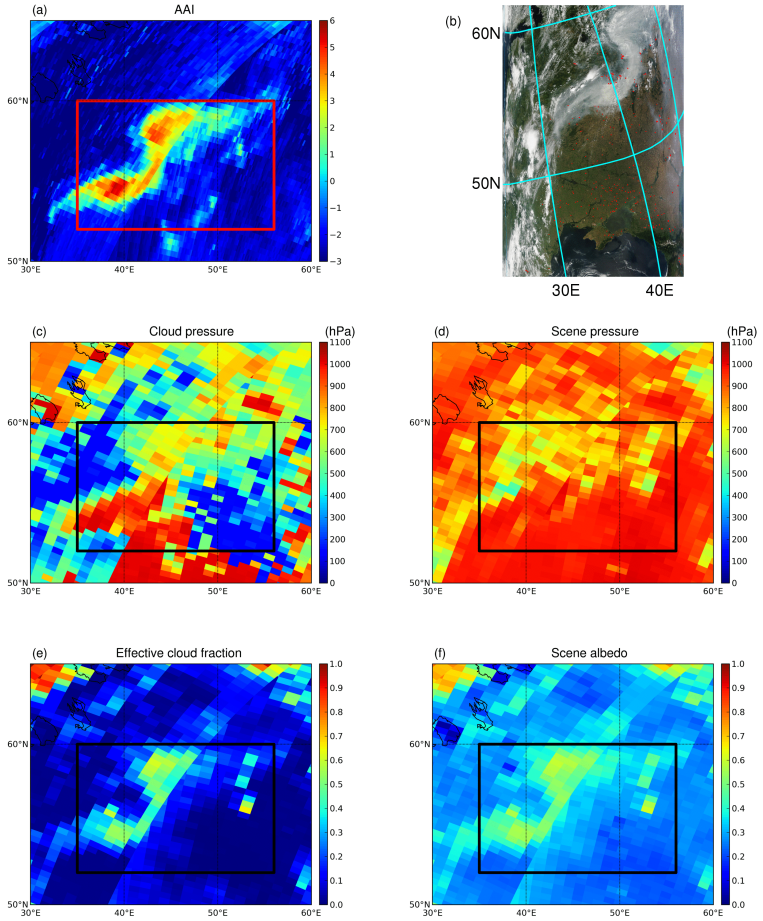

Fig. 12. **(a)** GOME-2 AAI image, **(b)** MODIS RGB image, **(c)** GOME-2 cloud pressure, **(d)** GOME-2 scene pressure, **(e)** GOME-2 effective cloud fraction, and **(f)** GOME-2 scene albedo for the smoke of Russian wild fires on 1 August 2010. The location of the plume is indicated with a box in the GOME-2 images. The plume in the box was measured around 06:50 UTC. The MODIS measurement is taken at 08:45 UTC. The red spots in the MODIS image indicate fires.

ACPD
11, 32685–32721, 2011

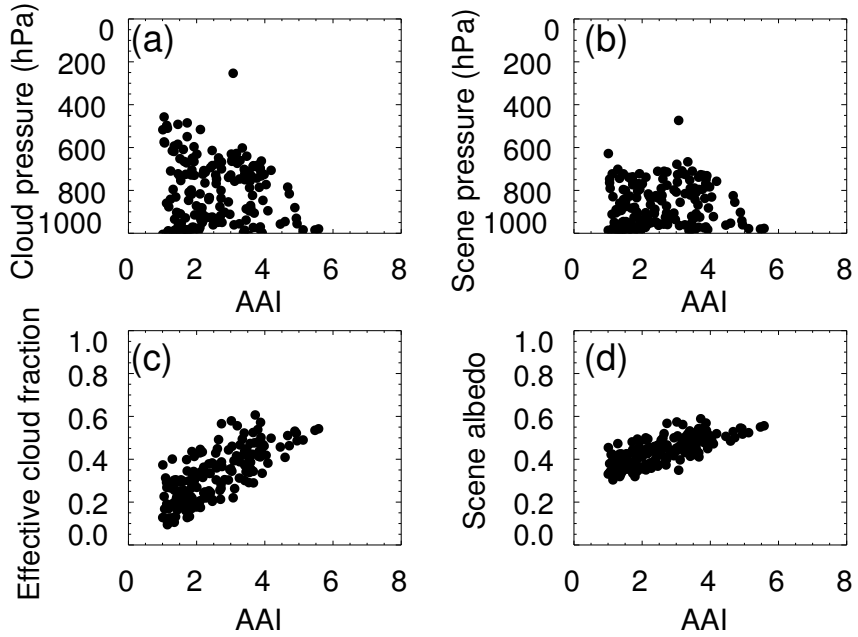

Fig. 13. Scatter plots of FRESCO **(a)** cloud pressure, **(b)** scene pressure, **(c)** effective cloud fraction, and **(d)** scene albedo versus absorbing aerosol index (AAI) from GOME-2 measurements of the Russian wild fire smoke event on 1 August 2010 around 06:50 UTC. The pixels used in the scatter plots are marked with a box in Fig. 12 in the region of [52, 60]° N and [35, 56]° E.

ACPD
11, 32685–32721, 2011